Electronic Supplementary Information

Novel Ba-hexaferrite structural variations stabilized on the nanoscale as building blocks for epitaxial bi-magnetic hard/soft sandwiched maghemite/hexaferrite/maghemite nanoplatelets with out-of-plane easy axis and enhanced magnetization

Blaž Belec, Goran Dražić, Sašo Gyergyek, Benjamin Podmiljšak, Tanja Goršak, Matej Komelj, Josep Nogués, Darko Makovec

Materials

Iron (III) nitratehepta hydrate ($Fe(NO_3)_3 \cdot H_2O$, iron (II) chloride ($FeCl_2$), magnesium hydroxide ($Mg(OH)_2$), urea (CH_4N_2O), barium nitrate ($Ba(NO_3)_2$), scandium nitrate ($Sc(NO_3)_2$), sodium hydroxide (NaOH), nitric acid (HNO_3), ammonia solution (NH_3, 25%), polyvinilpirolidone (PVP) were purchased from Alfa Aesar. A nitrate complex Fe^{3+}-urea ($[Fe((CO(NH_2)_2)_6(NO_3)_3]$), was synthesized according to the procedure described in the literature.[S1]

For comparison with the Sc-doped hexaferrite (BSHF) nanoplatelets the bulk Ba-Sc ceramics (BSHF bulk) were prepared by sintering the nanoplatelets. The nanoplatelets were pressed into compacts and sintered at 1200 ^oC for one hour (with heating and cooling rates of 20 $^oC\ min^{-1}$).

Characterization

X-ray diffractometry

The X-ray diffractometry (XRD) of the nanoparticles was performed using a PANalytical X` Pert PRO diffractometer.

Raman spectroscopy

Raman spectra of powdered samples were recorded with a NT-MDT model Integra Spectra for Materials Science, equipped with a confocal microscope, at room temperature. The 488 nm laser diode was used as excitation. The scattered light was detected by a cooled CCD camera and a 600 grooves mm^{-1} grating. The power density was approx. 5 mW. To obtain good signal-to-noise ratio and to prevent sample damage

several measuring conditions were tested. The first spectrum was acquired for 10 s, then the time was increased to 60 s and finally 10 spectra measured for 60 s were accumulated. At final spectrum at the same position was acquired for 60 s. The same procedure was repeated at different locations and the spectra were compared. Importantly, the spectra differ only in signal-to-noise ratios and absolute values of intensities, while the positions of bands and their relative intensities were always the same. The presented spectra were obtained by accumulating 10 spectra each acquired for 60 s, since they showed best signal-to-noise ratios.

Electron microscopy

For transmission (TEM) and scanning-transmission (STEM) electron microscopy studies, the nanoplatelets were suspended in ethanol and deposited on a copper-grid-supported lacy carbon foil. The TEM analyses were performed using a field-emission electron-source TEM Jeol 2010F equipped with an Oxford Instruments ISIS300 energy dispersive x-ray spectroscopy (EDXS) detector operated at 200 kV.

For the STEM analyses a probe Cs-corrected Jeol ARM 200CF STEM was operated at 80 kV. During the analysis of the samples, HAADF and ABF detectors were used simultaneously at 68–180 and 10–16 mrad collection semi angles, respectively. To minimize the specimen drift, images were taken several hours after the insertion of the sample in the microscope and at least 20 minutes after the last sample positioning to minimize the goniometer drift. The chemical composition was analyzed using a Jeol Centurio EDXS system with 100 mm^2 SDD detector and Gatan GIF Quantum ER Dual EELS system.

The simulated HAADF STEM images were calculated based on the atomic models for barium hexaferrite and maghemite and the microscope parameters using the quantitative STEM (QSTEM) code with a multi-slice method and frozen phonon approximation.[S2]

Magnetic measurements

The room-temperature magnetization $\boldsymbol{M}$ as a function of the magnetic field $\boldsymbol{H}$ of the samples was measured using a Lake Shore 7307 vibrating-sample magnetometer (VSM) with a maximum applied filed of 10 kOe. To prepare the specimens for the VSM measurements minimizing dipole-dipole interactions, nanoplatelets (~1 mg) were added into water (~2 mL) under intensive stirring. Then, sucrose (2 g) was dissolved in the suspension. After drying, the solid was heated to 160 °C to melt the sucrose. The

viscous suspension of nanoplatelets was rapidly cooled to solidify it. The obtained solid was milled and subsequently uniaxially pressed into cubic compacts. The magnetization of the cube compacts containing the nanoplatelets were measured with the magnetic field applied in three normal directions of the cube (along the pressing direction (x-axis) and perpendicular to the pressing direction (y-axis, z-axis)) using the VSM. The three measurements were averaged to obtain the magnetic properties of the randomly-oriented nanoplatelets.

To orient the nanoparticles for perpendicular and parallel magnetic measurements, the nanoplatelets were first hydrophobized by the adsorption of ricinoleic acid onto their surfaces and then a low concentration of nanoparticles was homogeneously dispersed in a liquid wax heated to 80 ^{o}C. While at 80 ^{o}C a homogeneous magnetic field of 10 kOe was applied and maintained while the wax was solidified by cooling.

The same VSM device was used for the temperature dependent measurements. Note that the nanoplatelets were coated with a silica shell prior to the measurements to minimize growth and excessive agglomeration at high temperatures. For the deposition of the silica shell onto the nanoplatelets a modified Stober process was used, as described in ref. S3.

The high temperature measurements where conducted under an argon atmosphere and a constant applied magnetic field of 200 Gauss. The magnetization was measured at different temperature intervals with a heating rate of 5 °C min^{-1} with a 1 min settling time. The Curie temperature was calculated from the thermomagnetic data, by finding the minimum of its temperature derivative.

Properties of hexaferrite nanoplatelets

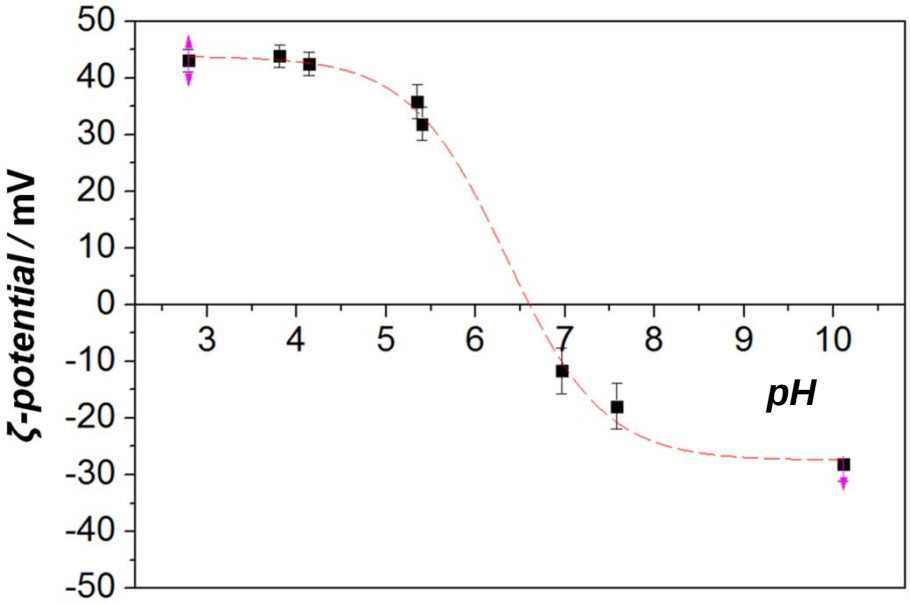

Fig. S1 ζ-potential of the BSHF nanoparticles as a function of the suspension pH.

Raman spectroscopy analysis of the composite nanoplatelets

Barium hexaferrite has a rich spectrum with 42 Raman active modes.[S4] All of the bands present in the spectrum of BSHF nanoplatelets (Fig. S2) are characteristic for the barium hexaferrite structure.[S4] However, after sintering the nanoplatelets into the ceramics two additional weak bands appeared at 228 cm^{-1} and 298 cm^{-1}. These two spectra can be ascribed to the presence of hematite,[S5,S6] which appeared in the ceramics due to deviation of the BSHF nanoplatelets structure and the composition from the bulk composition.

The Raman spectrum of maghemite nanoparticles M shows bands at positions characteristic of iron oxide having a maghemite structure.[S5,S6] There are three Raman active lattice vibrations that give rise to three bands having a broad structure.[S6] The distinction between maghemite and magnetite, which shows richer Raman spectra is in position of the bands, which are in case of magnetite shifted to lower wavenumbers by at least 30 cm^{-1}.[SI6] The difference in bands position for the maghemite and the magnetite is significantly larger than spectral resolution. Composite nanoplatelets CNP1.9 show additional band at approximately 380 cm^{-1} which is absent in the spectrum of the BSHF

and is not characteristic of the barium hexaferrite structure. Additional band is very close to the maghemite characteristic band found in the spectrum for maghemite nanoparticles M positioned at 350 cm^{-1}. This band is the only one in maghemite that is not overlapping with the bands of barium hexaferrite. Also in the CNP1.9 spectrum the band at approx. 300 cm^{-1}, where the strong band is observed in magnetite, is absent.[S6] We believe that this is a firm evidence that the spinel layer at the hexaferrite core of the composite nanoplatelets crystalizes in the maghemite structure.

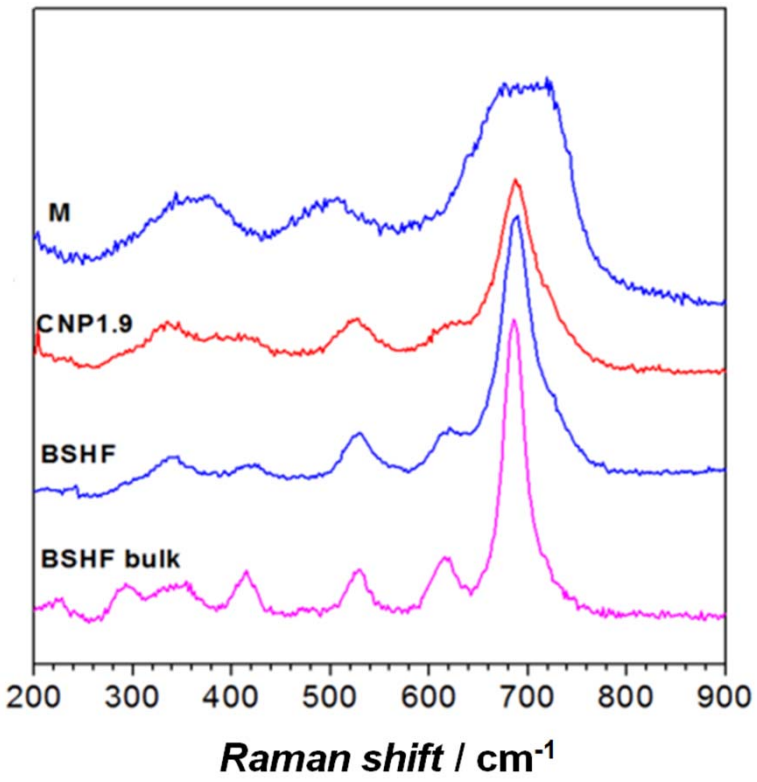

Fig. S2 Raman spectra of the maghemite nanoparticles (M), hexaferrite core nanoplatelets (BSHF), hexaferrite ceramics (BSHF bulk), and the composite nanoplatelets CNP1.9.

TEM analysis of the composite nanoplatelets synthesized using too large Fe/HF ratio

When the Fe/HF molar ratio exceeded 5.4 individual larger maghemite nanoparticles form in the samples. Fig. S3 shows a TEM image of the sample synthesized using the Fe/HF molar ratio of 8.1. Some large maghemite nanoparticles are marked with arrows.

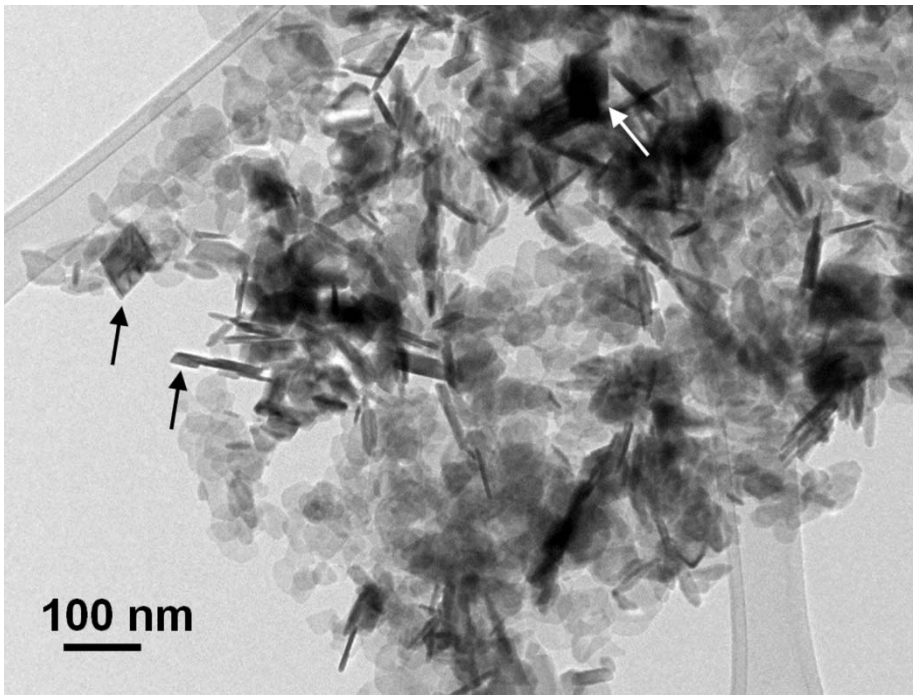

Fig. S3 TEM image of composite nanoparticles synthesized using Fe/HF = 8.1. Large maghemite nanoparticles are marked with arrows.

Analysis of the composite nanoplatelets CNP2.5

In the CNP2.5 sample synthesized by deposition of maghemite layers onto the BSHF nanoplatelets in the two-step procedure, asymmetric composite nanoplatelets were occasionally found. Fig. S4 shows HRTEM image of one such asymmetric composite nanoplatelets.

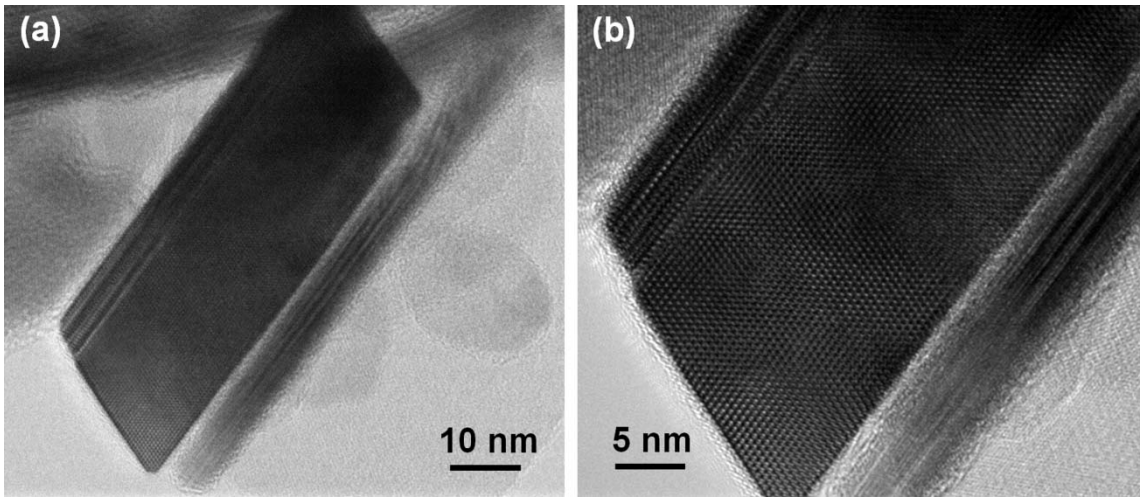

Fig. S4 HRTEM images of an asymmetric composite nanoparticle in the CNP2.5 sample ($<10\text{-}10>_{HF}$ || $<101>_{M}$).

Even when the composite nanoplatelets were synthesized in the two-step process (sample CNP2.5) the maghemite deposited exclusively as epitaxial layers on both the basal surfaces of the hexaferrite core nanoplatelets, while the side surfaces were always free of any deposited material. Fig. S5 shows a HAADF STEM image of the composite nanoplatelet in the sample CNP2.5. A comparison of the experimental image with the superimposed projected hexaferrite structural model shows that the atomic columns on the side of the hexaferrite core can be ascribed to the hexaferrite structure on the very surface.

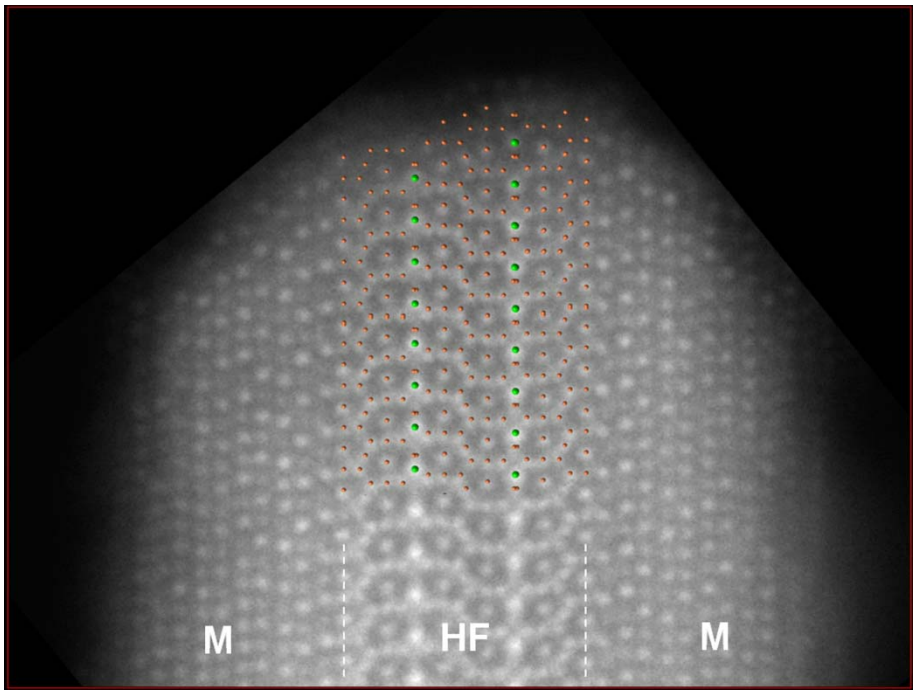

Fig. S5 HAADF STEM image of a composite nanoplatelet in the CNP2.5 sample with the superimposed hexaferrite projected structure ($<10\text{-}10>_{HF} \parallel <101>_{M}$).

Quantitative EDXS analyses of the core nanoplatelets

The composition of the BSHF nanoplatelets were compared with the composition of larger platelet crystals of the same $BaFe_{10.5}Sc_{1.5}O_{19}$ nominal composition that were used as a "bulk" standard. The platelet crystals, 0.5-2 μm wide (Fig. S5) were synthesized using the same hydrothermal method as for the nanoplatelets, just with much longer time (24 hours) at the final temperature (240 ^{o}C). The thickness of the platelet crystals lying flat on the specimen support was estimated by computation of the zero loss electron energy loss spectroscopy (EELS) spectra to be just over 10 nm. The spectrum taken at the large platelet crystals was used as a standard during quantization of the spectra collected at the nanoplatelets. The relative error of the Fe+Sc/Ba ratio, tested on the large platelet crystals was estimated to be less than ± 6 %.

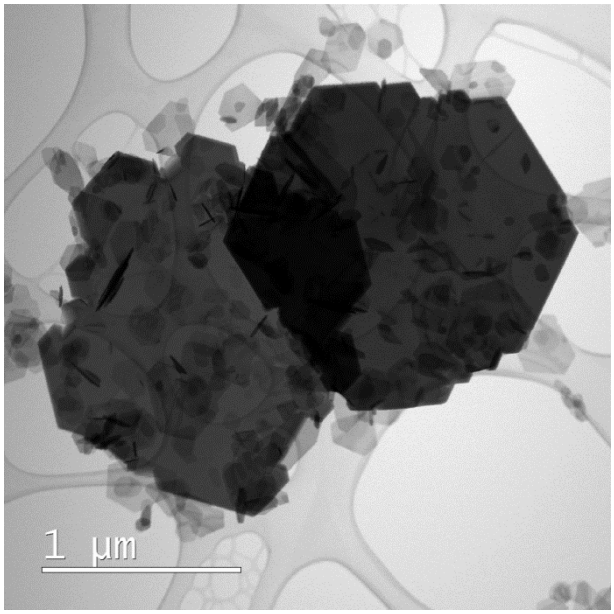

Fig. S6 BF STEM image of platelet crystals used as a "bulk" standard for EDXS analyses.

Ab-initio calculation

To explain the reason for the experimentally-observed S-block-termination by means of the energetically most favorable structure we performed *ab-initio* simulations within the framework of the density-functional theory. The idea was to compare the calculated total energies E_{tot} for several S- and R-terminated structures, which all consist of a fixed number of the Ba, Fe and O atoms, and to determine the most stable one with the minimum E_{tot}. The calculations were carried out by applying the Quantum-Espresso code[S7] with the generalized-gradient approximation (GGA)[S8] of the exchange-correlation potential. The interaction between the valence and the core electrons was described by the Troullier-Martins-type[S9] pseudopotential. All considered structures were optimized by relaxing the atomic positions in terms of minimizing the total energies and inter-atomic forces. The plane-wave and the charge-density cut-off parameters were set to 204 eV and 816 eV, respectively. The Brillouin-zone integration was carried over 4x4x1 **k**-points evenly distributed on the Monkhorst-Pack mesh[S10]. The criterion for the self-consistency was the total-energy difference between the two subsequent iterations being less than 10^{-9} Ry. The structures were considered as relaxed when the magnitudes of all inter-atomic forces were less than 10^{-3} Ry/a.u., where a.u. stands for the Bohr radius. The thickness d_{vac} of the vacuum was half of the slab thickness, in the case of the structures presented in **Fig. S6** d_{vac}=11.6 a.u..

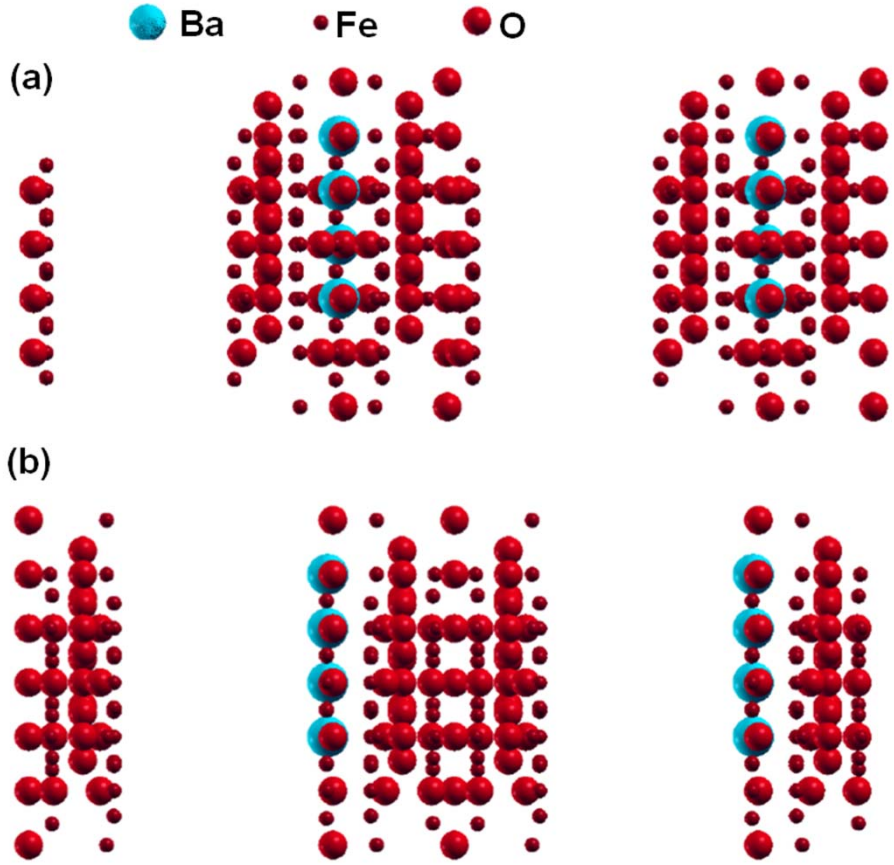

Fig. S7 An example of the modeled HF structures terminated by the Fe-only a) and Fe-Ba b) surfaces. The calculated total energy of the (b) structure is 127 meV/atom lower than the total energy of the (a) structure.

Magnetic measurements of physical mixtures of hexaferrite nanoplatelets and maghemite nanoparticles

To clearly show the difference between the magnetic properties of the exchange-coupled composite nanoplatelets and the hysteresis of a physical mixture of the hard-magnetic and the soft-magnetic phases, the hysteresis loop of a mixture of BSHF nanoplatelets and maghemite (M) nanoparticles was measured. As the soft phase pherical M nanoparticles, 9.7±1.5 nm in diameter, were chosen (Fig. S7). The volume of the M nanoparticles was comparable to that of the maghemite layers of the CNP1.9 composite nanoplatelets. First, the two types of the magnetic particles were dispersed in sucrose, as explained above. Then, the two magnetic-particles-containing sucrose powders were mixed together in a M/BSHF mass ratio of 1, corresponding to the estimated composition of CNP1.9.

Fig. S8 shows the hystereses loops for the hard-magnetic BSHF core nanoparticles, soft-magnetic M nanoparticles and their physical mixture (BSHF + M). Red dashed loop represents the sum of the hysteresis loops for the two magnetic components (red loop), calculated using the formula $\boldsymbol{M_{mix}(H) = 0.5\, M_{BSHF}(H) + 0.5\, M_{M}(H)}$. Note that the mixture BSHF + M shows the characteristic constricted hysteresis loop for two phases that magnetize independently.

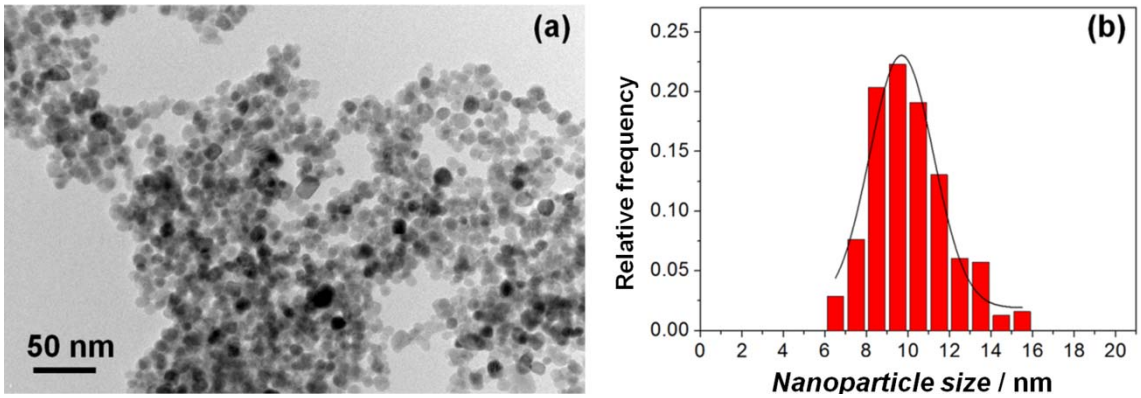

Fig. S8 TEM image (a) and particle size distribution (b) of maghemite M nanoparticles used as soft-magnetic phase for magnetic measurements of the physical mixtures.

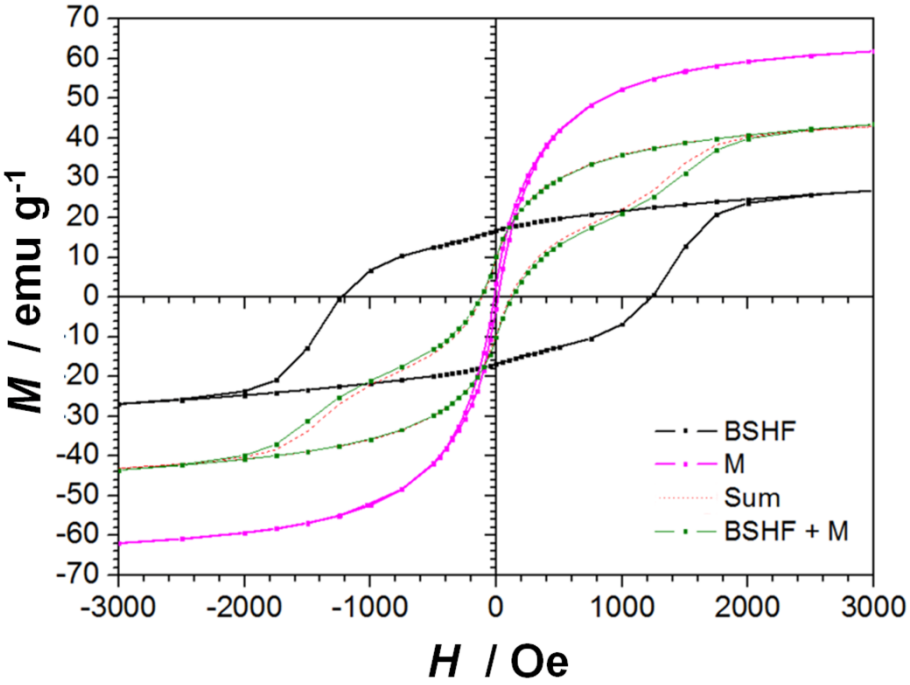

Fig. S9 Magnetic hystereses for the BSHF nanoplatelets, the M nanoparticles and their physical mixture.

Properties of the composite nanoplatelets composed of hexaferrite core coated with non-magnetic zinc-ferrite layers

To assess the influence of the epitaxial layers on the magnetic properties of the BSHF nanoplatelet core, non-magnetic zinc-ferrite layers were deposited instead of γ-Fe_2O_3. The zinc ferrite was deposited using the same procedure as used for synthesis of the CNP1.9, except that $FeCl_2$ was replaced by $ZnCl_2$. The TEM analysis (Fig. S9) showed only composite nanoplatelets (without any uncoupled ferrite particles), while EDXS analysis in the STEM confirmed that each nanoplatelet contained Zn. Elemental mapping recorded by EDXS in STEM (Fig. S10) clearly shows presence of Zn in the layers. Note that similar to the of γ-Fe_2O_3 layers, the Zn-ferrite also grows epitaxially on the BSHF platelets (Fig. S10).

In bulk, zinc ferrite ($ZnFe_2O_4$) is paramagnetic at room temperature, as the tetrahedral A sublattice of its normal spinel structure is almost exclusively populated by the non-magnetic Zn^{2+} ions.[S11,S12] However, in nanostructured form, zinc ferrite becomes weakly ferrimagnetic, as a significant proportion of the Fe^{3+} ions exchanges sites with the Zn^{2+} ions, i.e., it adopts a partially inverted spinel structure.[S13] Spherical zinc-ferrite nanoparticles of approximately 8 nm display superparamagnetism with $\boldsymbol{M_S}$ of approximately 8 emu/g (measured at 13.8 kOe).[S13] With annealing at temperatures above approximately 400 ^{o}C in air, their structure rearrange to the equilibrium ‘‘bulk’’ state and the nanoparticles became paramagnetic.[S13] The measurement of the Zn-ferrite based composite nanoplatelets, ZnCNP, with approximately 1.9 nm thick zinc-ferrite layers showed a single-phase hysteresis loop (Fig. S11). The $\boldsymbol{M_S}$ of the as-synthesized ZnCNP was lower to that of the BSHF nanoplatelets indicating weakly magnetic layers. Estimation of the $\boldsymbol{M_S}$ of zinc ferrite considering its mass fraction in the composite ($\boldsymbol{w_{layer}}$ □ 0.5) gave $\boldsymbol{M_{S(layer)}}$ of approximately 13 emu/g. However, annealing the ZnCNP at 500 ^{o}C the $\boldsymbol{M_S}$ of the ZnCNP decreased almost to the half of the one of the BSHF nanoplatelets, indicating that the zinc ferrite became nearly paramagnetic. Moreover, the zinc-ferrite layers had pronounced influence on the $\boldsymbol{H_C}$ of the composite nanoplatelets, which exhibit considerably smaller $\boldsymbol{H_C}$ than the BSHF core. Given the non-magnetic character of zinc-ferrite, the most plausible origin for the $\boldsymbol{H_C}$ decrease is the structural stresses induced on the core by the epitaxial surface layers.

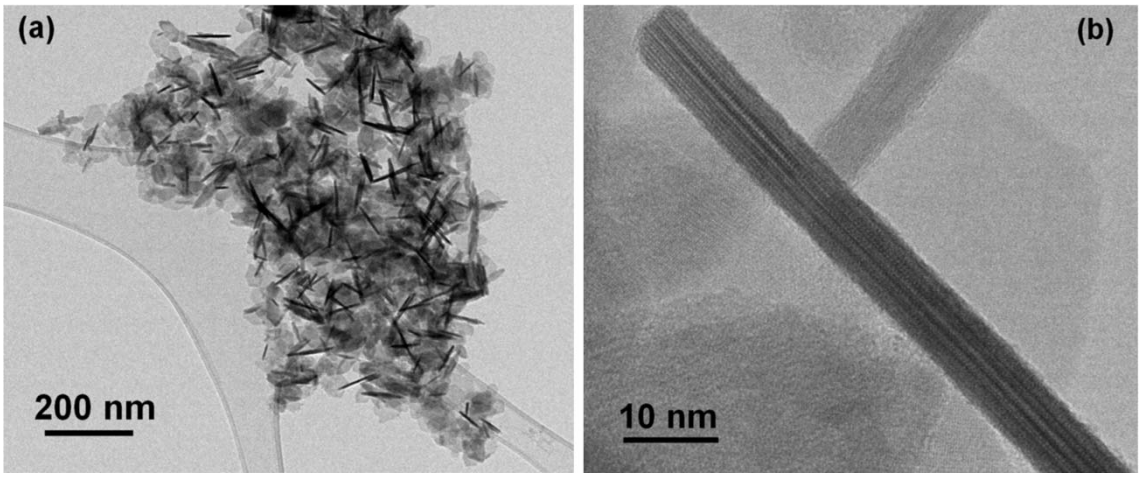

Fig. S10 TEM (a) and HRTEM (b) images of the ZnCNP nanoplatelets.

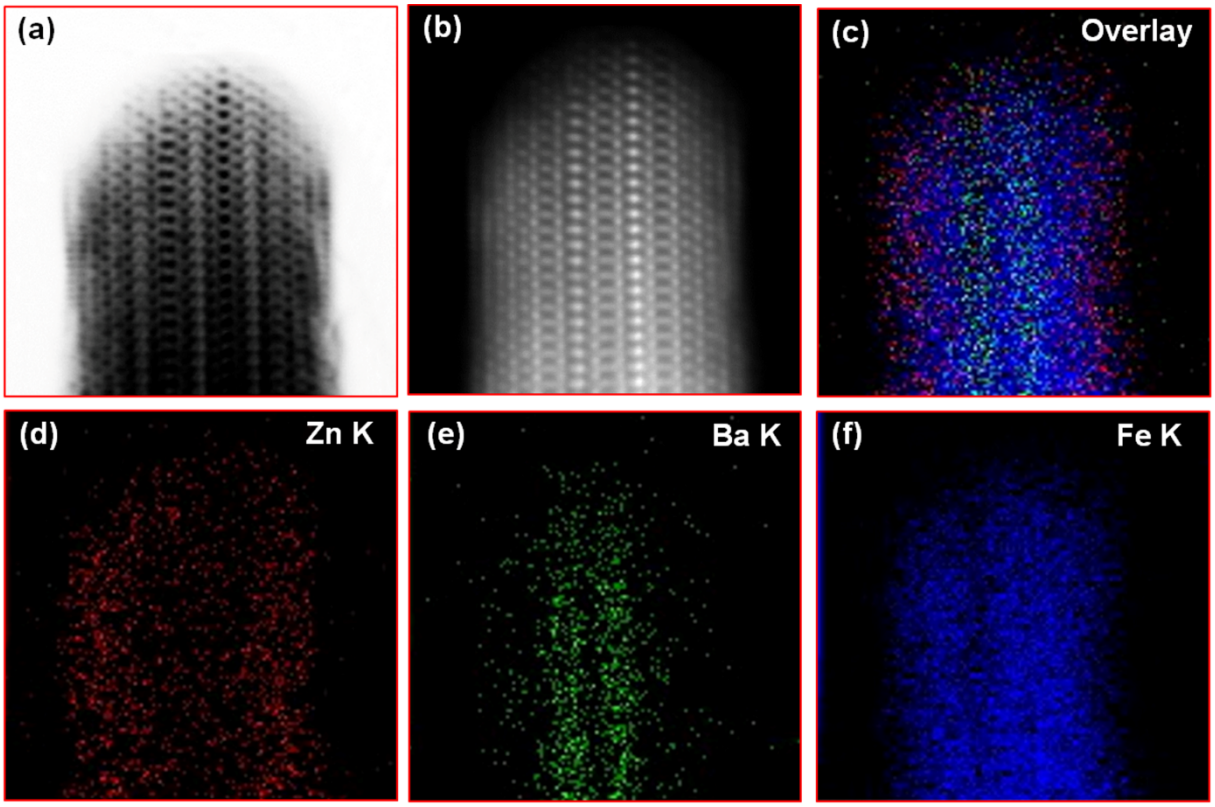

Fig. S11 BF (a), HAADF (b) STEM images and the corresponding EDXS elemental mappings (c-f) of the composite ZnCNP nanoplatelet oriented with its hexaferrite (HF) core along $<11\text{-}20>_{HF}$.

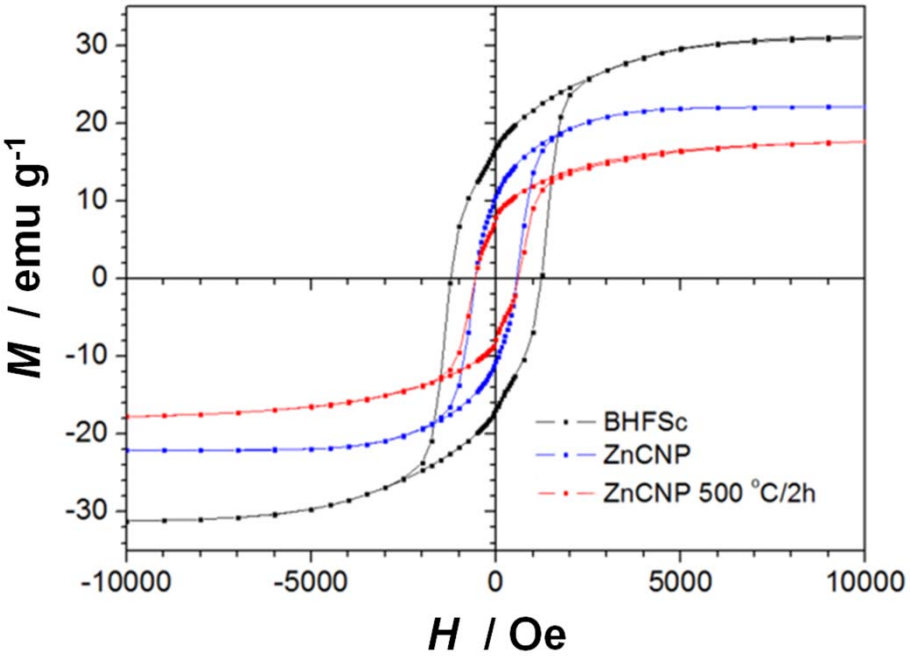

Fig. S12 Hystereses loops for the BSHF core nanoplatelets and the composite nanoplatelets ZnCNP, before and after annealing.

High-temperature magnetic measurements

To minimize growth and excessive agglomeration of the nanoplatelets during the high-temperature magnetic measurements they were coated with thin layer of silica, SiO_x,. The BSHF core nanoplatelets were coated with ~ 8 nm thick silica layer (Fig. S12), whereas the coating was thinner at the CNP1.1 nanoplatelets, approximately 3 nm (Fig. S13).

Room temperature hysteresis loops were measured for both samples (Fig. S14) before and after the *M*(T) measurements up to 550 ºC (Fig. 4c) . It can be seen that while the magnetic properties of the BSHF core nanoplatelets only change slightly (perhaps due to some strain relieve after reaching 550 ºC), the ones for the CNP1.1 nanoplatelets are markedly different before and after the M(T) measurements. The large change in $\boldsymbol{M_S}$ and $\boldsymbol{H_C}$ hint a possible structural transition CNP1.1 nanoplatelets after the high temperature treatment.

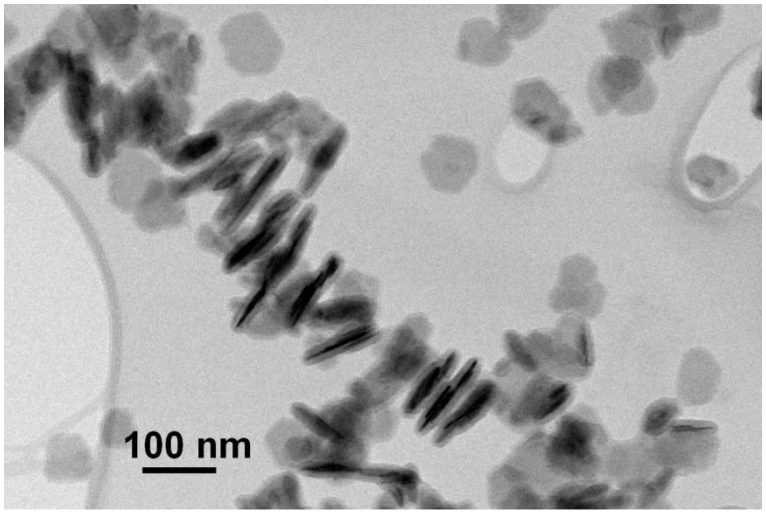

Fig. S13 TEM image of the silica-coated BSHF nanoplatelets

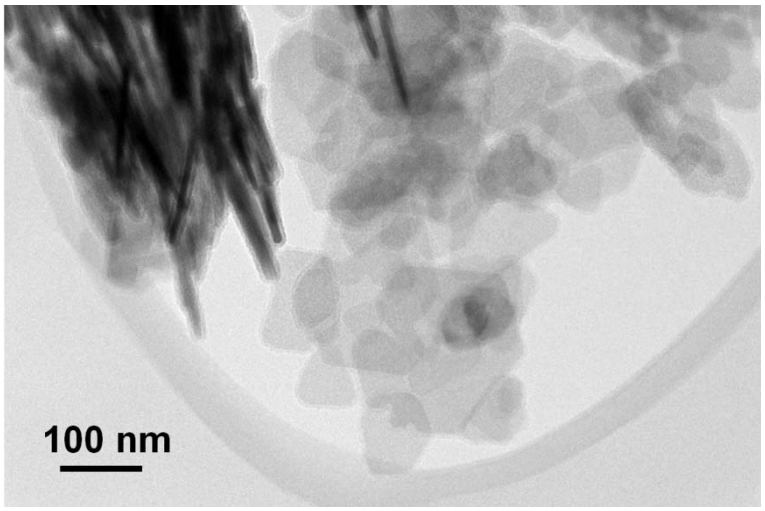

Fig. S14 TEM image of the silica-coated CNP1.1 nanoplatelets.

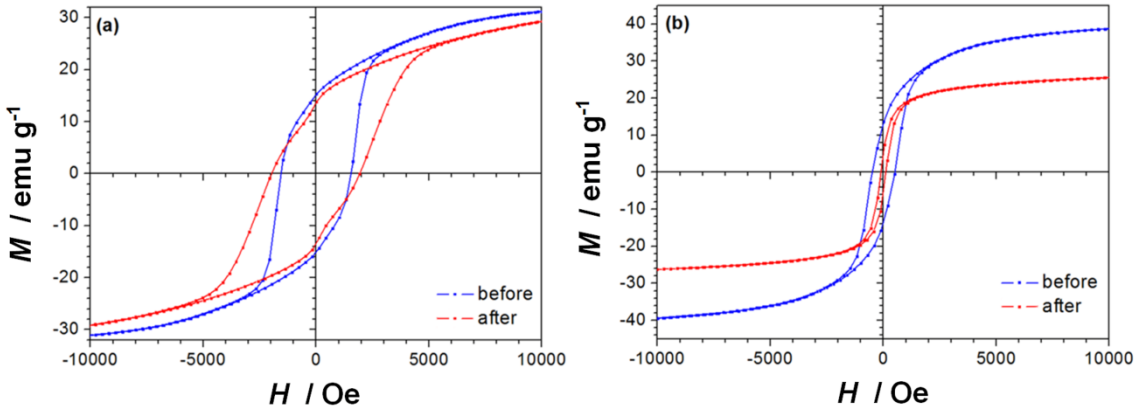

Fig. S15 Room-temperature magnetic hysteresis loops for the silica coated BSHF (a) and CNP1.1 (b) nanoplatelets measured before and after the high temperature measurements.

References

S1. S. Asuha, S. Zhao, X. H. Jin, M. M. Hai and H. P., Bao, *Appl. Surf. Sci.*, 2009, **255**, 8897-8901 .

S2. K. Koch, Determination of Core Structure Periodicity and Point Defect Density along Dislocations, Arizona State University, 2002.

S3. S. Kralj, D. Makovec, S. Čampelj and M. Drofenik, *J. Magn. Magn. Mater.*, 2010, **322**, 1847–1853.

S4. J. H. Monkhorst and J. D. Pack, *Phys. Rev. B.*, 1976, **13**, 5188-5192.

S5. R. M. Cornell, U. Schwertmann, *The Iron Oxides: Structure, Properties, Reactions, Occurrences and Uses,* Wiley-VCH, Weinheim, Germany, **2003**.

S6. I. Chamritski, G. Burns, *J. Phys. Chem. B*, 2005, **109**, 4965-4968.

S7. Giannozzi, P., Baroni, S.,, Bonini, N., Calandra, M:, Car, R., Cavazzoni, C., D. Ceresoli, G.L. Chiarotti, M. Cococcioni, I. Dabo, A.D. Corso, S. de Gironcoli, S. Fabris, G. Fratesi, R. Gebaurer, U. Gerstmann, C. Gougoussis, A. Kokalj, M. Lazzeri, L. Martin-Samos, N. Marzari, F. Mauri, R. Mazzarello, S. Paolini, A, Pasquarello, L. Paulatto, C. Sbraccia, S. Scandolo, G. Sclauzero, A.P. Seitsonena, A. Smogunov, P. Umari and R.M. Wentzcovitch, *J. Phys. Condens. Matte*, 2009, **21**, 395502.

S8. J. P.Perdew, K. Burke and M. Ernzerhof, M. Phys. Rew. Lett., 1996, 77, 3865-3868.

S9. N. Troullier and J.L. Martins, Phys. Rev. Lett., 1991, 43, 1993-2006.

S10. J. H. Monkhorst, J. D. Pack, *Phys. Rev. B.*, 1976, **13**, 5188-5192.

S11. H. S. O'Neill, Eur. *J. Mineral.*, 1992, **4**, 571-580.

S12. D. Makovec, A. Kodre, I. Arčon, *J. Nanopart. Res.*, 2011, **13**, 1781-1790.

S13. D. Makovec and M. Drofenik, *J. Nanopart. Res.*, 2008, **10**, 131-141.